A current-driven resistive instability and its nonlinear effects in simulations of coaxial helicity injection in a tokamak

E. B. Hooper and C. R. Sovinec

Citation: Physics of Plasmas **23**, 102502 (2016); doi: 10.1063/1.4964292
View online: http://dx.doi.org/10.1063/1.4964292
View Table of Contents: http://scitation.aip.org/content/aip/journal/pop/23/10?ver=pdfcov
Published by the AIP Publishing

A current-driven resistive instability and its nonlinear effects in simulations of coaxial helicity injection in a tokamak

E. B. Hooper[1] and C. R. Sovinec[2]
[1]Woodruff Scientific, Inc., 4000 Aurora Ave. N, Suite 6, Seattle, Washington 98103, USA
[2]Department of Engineering Physics, University of Wisconsin-Madison, Madison, Wisconsin 53706-1609, USA

(Received 28 July 2016; accepted 21 September 2016; published online 6 October 2016)

An instability observed in whole-device, resistive magnetohydrodynamic simulations of the driven phase of coaxial helicity injection in the National Spherical Torus eXperiment is identified as a current-driven resistive mode in an unusual geometry that transiently generates a current sheet. The mode consists of plasma flow velocity and magnetic field eddies in a tube aligned with the magnetic field at the surface of the injected magnetic flux. At low plasma temperatures (~10–20 eV), the mode is benign, but at high temperatures (~100 eV) its amplitude undergoes relaxation oscillations, broadening the layer of injected current and flow at the surface of the injected toroidal flux and background plasma. The poloidal-field structure is affected and the magnetic surface closure is generally prevented while the mode undergoes relaxation oscillations during injection. This study describes the mode and uses linearized numerical computations and an analytic slab model to identify the unstable mode. [http://dx.doi.org/10.1063/1.4964292]

I. INTRODUCTION

Magnetic helicity injection[1,2] has been used extensively to drive current in tokamaks and spheromaks. Injection into a strong toroidal field can form a tokamak configuration through relaxation processes or through transient effects. In the former, magnetic reconnection and relaxation driven by large amplitude, global modes, especially toroidal mode number $n=1$ and poloidal mode number $m=1$, convert injected toroidal flux into poloidal flux at near-constant helicity ("flux amplification"). For experimental results, see Ref. 3 and references therein; the process is essentially the same as that operated in spheromaks (e.g., Refs. 4–6 and references therein). Alternate interpretations of the fluctuations are offered in Refs. 7 and 8, but we note that magnetohydrodynamic (MHD) fluctuations are present whenever poloidal flux is actively amplified.

A plasma formation process (coaxial helicity injection, CHI) has been explored in the National Spherical Torus eXperiment, NSTX, to generate plasma in which open field lines reconnect to form closed magnetic surfaces. The amount of injected helicity is relatively low, and the process is both dynamic and nearly axisymmetric. The goal is to form the plasma suitable for initiating the full tokamak discharge.[9,10] Two-dimensional simulations of this formation using the NIMROD code[11] found that the reconnection agreed well with the Sweet-Parker model.[12,13]

Whole-device, three-dimensional resistive MHD simulations of the NSTX helicity injection experiments[14] not only reached a similar conclusion about reconnection but also found a low-level, non-axisymmetric mode ($n=1$, high m) during the driven phase. It saturated benignly with little effect on the injection or the formation of closed surfaces. This high poloidal-mode number, non-axisymmetric mode was also observed (unpublished) in simulations during early phases of injection into spheromaks. However, as discussed below, in simulations of injection in the NSTX geometry, the mode can become strong enough that its amplitude has a bursting characteristic, repetitively growing and collapsing. Our simulations show that this process can have an appreciable effect on the axisymmetric equilibrium during injection, e.g., broadening the current layer that is associated with the expanding flux bubble, precluding flux closure during the driven phase, and altering energy and flow evolution. The study does not include the stage when power is reduced as in NSTX experiments and does not preclude flux-surface closure in transient coaxial helicity injection, TCHI.[9,10] These dynamics are achieved at high plasma temperature, which is intentionally induced by lowering the impurity density to investigate high helicity-injection rates in a clean, wall-conditioned tokamak.

Apart from its potential relevance to an upgraded configuration, the detailed physics of the mode is also of interest in itself. It consists of a current-driven reconnecting mode in the unusual geometry of a narrow current sheet along the expanding surface that bounds injected toroidal flux. This bubble of current exists while helicity is injected through the coaxial electrodes. The mode assessment includes linearized stability calculations for an axisymmetric bubble configuration, and the results show a growing linear mode with a structure that is very similar to the instability in the nonlinear simulation. The growth rate of the linear mode is found to depend on viscosity and resistivity, and weakly on particle diffusivity but these have little qualitative effect on the mode structure. The axisymmetric velocity field also affects the mode but a strong growth persists in the absence of the flow. An analytical, slab model with a current layer finds a reconnecting mode with peak amplitude in the center of the sheet and wavenumbers along the sheet smaller than the inverse of

the current layer width. When considering the large surface area of the current-sheet bubble that surrounds the injected toroidal flux, the analytical findings are consistent with the large m observed in simulations. The magnetic field eddies are similar to those in the MHD simulations and linearized, numerical stability calculations. The structure is reminiscent of the current-sheet instability that underlies plasmoid instability.[15–19] However, unlike basic-physics studies of magnetic reconnection and simulations of axisymmetric flux closure in NSTX,[18,19] the current sheet surrounding the early evolution of the flux bubble is not associated with large-scale reconnection.

The whole-device NIMROD simulations used herein are in the single-fluid, resistive regime. The plasma model is very similar to that used in simulations of the SSPX spheromak. Apart from the CHI injector and absorber gaps, the machine boundary is modeled as an electrical conductor with the normal component of the magnetic field held constant. The injector-gap boundary condition applies time-dependent voltage (tangential electric field), modeling the CHI circuit in NSTX, and the boundary condition for RB_ϕ along the absorber gap prevents net current across the gap. The normal component of velocity on the boundary is zero except across the two gaps, where it is set to the $\mathbf{E}\times\mathbf{B}$ velocity. A detailed summary of the parameters and assumptions can be found in Refs. 14 and 20 including the modifications of the resistive-MHD, spheromak model for tokamak helicity-injection.

Section II of this paper provides an overview of the previously reported numerical instability results for injection into the NSTX geometry and briefly compares axisymmetric and non-axisymmetric simulations pertinent to the present work. It describes the nonlinear mode characteristics and its effects on the axisymmetric current distribution. Section III presents the results of the linearized NIMROD computations and the slab instability model. The results and their implications are summarized in Section IV.

II. OVERVIEW OF NONLINEAR SIMULATION RESULTS

A. Injection mechanism and impurity modeling

The injection geometry and the resulting poloidal-flux geometry ("flux bubble") are shown in Fig. 1. Voltage is applied across the axisymmetric slot in the bottom of the spherical tokamak, injecting plasma, and helicity at the local $\mathbf{E}\times\mathbf{B}$ velocity. Current flows in a layer along the surface of the flux bubble, generating a jump in magnetic fields across the layer. The bubble's expansion is driven by the associated $\mathbf{j}\times\mathbf{B}$ force or, equivalently, the magnetic pressure difference due to the change in field across the current layer.

The instability analyzed in this report forms a tube, seen in Fig. 1(c), along the magnetic field.[21] The mode forming the tube consists of poloidal velocity and magnetic field eddies with their axes aligned along the total (toroidal plus poloidal) magnetic field, as described later. Because this mode is only active during injection, the simulations reported here focus on plasma evolution during injection and do not model the important post-injection transient.

The vacuum poloidal flux in the simulation is that generated by magnetic coils used in the experiment. For the present case, the total vacuum poloidal magnetic flux in the machine cross section is approximately 0.55 Wb. However, the simulated plasma dynamics only incorporates about 22 mWb in the flux bubble after 1.5 ms, at which time the bubble has expanded to 70% of the machine height. The structure of the poloidal flux is similar to that shown in Fig. 1(b). The voltage across the helicity-injection slot is about 450 V and the discharge current is about 1.5 kA; both change in response to the plasma impedance during the simulation.

The primary difference between the present results and the whole-device simulations that were compared with flux-closure in the experiment[14] is a reduction in the modeled impurity density and thus the plasma radiative cooling. The simulations use an impurity-radiation model based on oxygen,

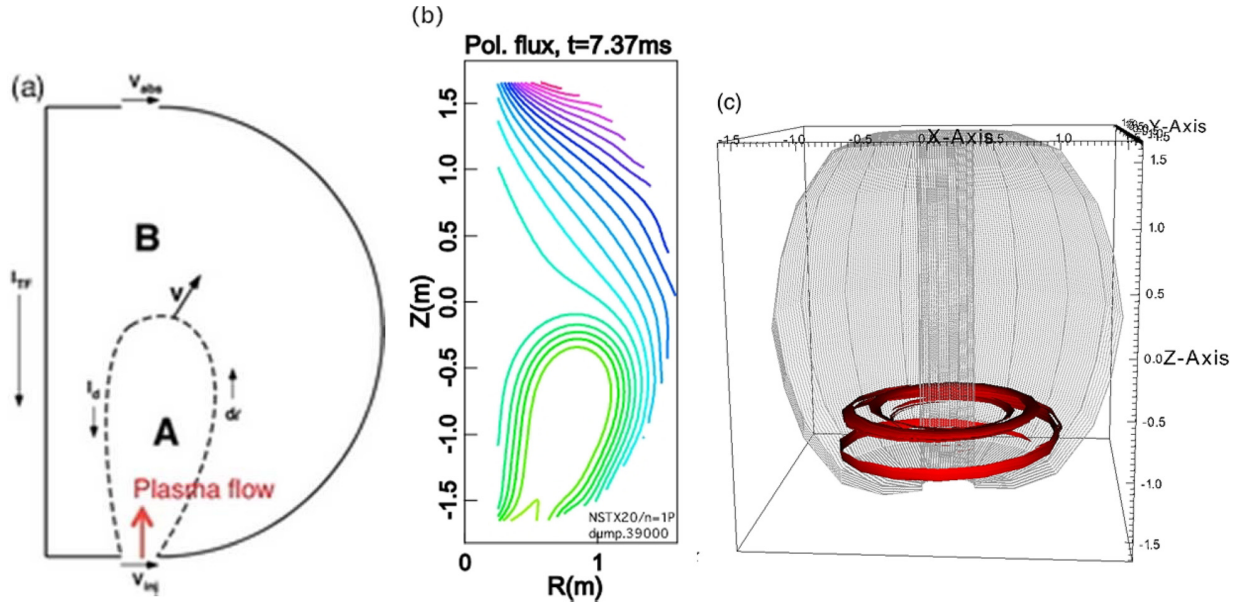

FIG. 1. (a) Helicity injection geometry, (b) resulting poloidal-flux structure, and (c) unstable mode on surface of the flux bubble—shown is a surface of constant flow speed.

which previously kept the plasma temperatures comparable to TCHI experiments in NSTX (~10–25 eV). The impurity model uses the calculations by Post *et al.*[22] In the present calculations, the impurity density is taken to be comparable to the electron density in the lower-left corner of the tokamak vessel where the injected current strikes and the electron temperature is low, dropping off away from the corner as a Gaussian with characteristic lengths of 0.45 m (radial) and 1.0 m (vertical). Radiation from oxygen has a strong peak at about 25 eV; the large impurity density needed in Ref. 14 to match the experiment likely includes the effects of transient ionization of sputtered impurities and any higher Z impurities. In the present work, the relatively high temperature (~100 eV) in the current channel effectively burns-out the remaining oxygen, reducing radiative cooling significantly.

The thermal conduction along magnetic-field lines uses the Braginskii model, and the values are very high away from the walls. Across the magnetic field, a constant value of 5 m^2/s is assumed. Early in the study, preliminary simulations were done varying this value up to 20 m^2/s; the results were insensitive to the value.

The simulations presented here may be important for a very clean machine, with little impurity generated from the wall strike-points of the current associated with the helicity injection.[14] The applied injection voltage has not been reduced from previous simulations; a reduction would drop the injection rate and the current and temperature in the current channel, suggesting a possible means to minimize any negative consequences of the mode.[23]

B. Nonlinear simulations

First, consider the results from axisymmetric simulations during helicity injection. The simulations start at 6.0 ms for consistency with the start of injection in the experiment. Injection ends at 9.0 ms.

The helicity-injection gap width on the bottom of the plate is 4 cm, which is the same as in the experiments[9,10] and the previous whole-device simulations in Ref. 14, and the bias poloidal magnetic field strength and geometry are the same as used in the experimental discharge 142163. The operating point (discharge voltage and current) is determined by a model of the experimental power supply with the plasma setting the time-varying load impedance. For the parameters used here (density, thermal conductivity, radiation losses, and their spatial distribution, etc.), the injected current flows primarily in a layer at the surface of the expanding, injected "flux bubble." The temperature is low ($\leq$5 eV) except in the current layer. As a result, in axisymmetric simulations resistive formation of an X-point occurs in the slowly evolving, low-temperature region. In the case shown in Fig. 2, such an X-point is seen at $R \approx 0.5$ m and $Z \approx -1.1$ m. Note that the gradient of poloidal flux contours in the core plasma is much less than those in the current-carrying surface and outside the bubble. (The contours are close enough together to be blurred except in the core.)

As the injection continues, the X-point moves out in radius and upward in *Z*. Fig. 3 shows the location at the end of injection (3 ms into the simulation). The field geometry

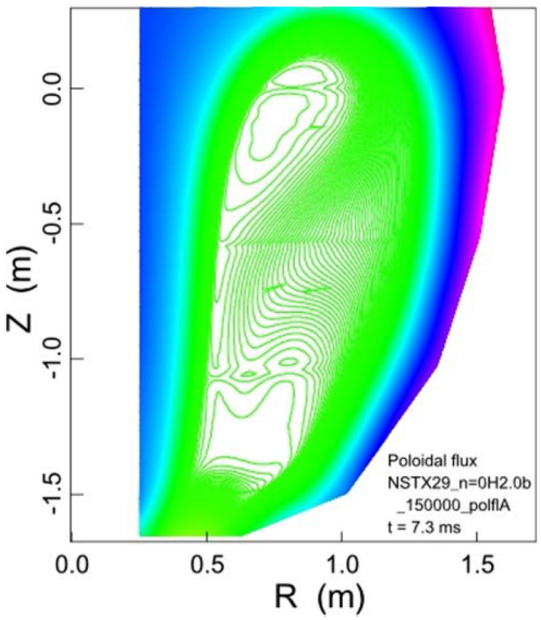

FIG. 2. X-point formation during injection in the axisymmetric approximation. The simulation has reached 1.3 ms from the start of injection, with the injected flux filling approximately 50% of the machine height. These simulations use a 45×90 mesh of finite elements over the poloidal plane with 5th order polynomial basis functions.

associated with the separatrix deflects the plasma flow outward from the injection slot, and closed flux surfaces form.

Next, a series of nonlinear simulations using identical injection parameters but with different sets of toroidal Fourier components, i.e., different levels of toroidal resolution, are used in the present study of the instability: (a) ($n = 0I$) axisymmetric,

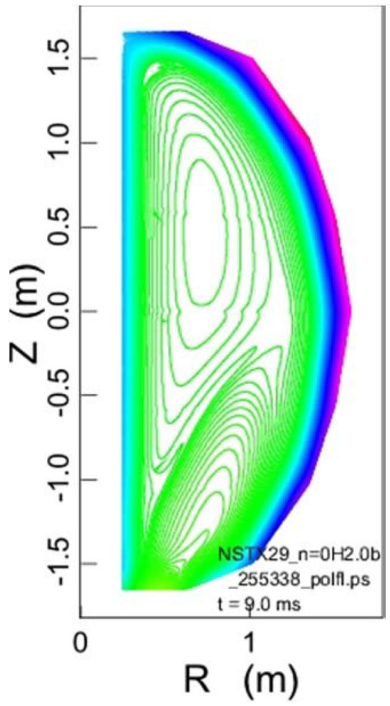

FIG. 3. X-point at 9 ms (3 ms from the start of injection) for the simulation in Fig. 2. The X-point has moved radially and vertically and is at $R \approx 1.1$ m and $Z \approx 0.0$ m. This isolates the closed flux region to the left and above the X-point from the flow through the injector slot.

$n=0$ mode only; (b) ($n=1I$) non-axisymmetric, $n=0$ and 1 modes; and (c) ($n=2I$) non-axisymmetric, $n=0$, 1, and 2 modes. Another simulation (not included here) had modes $n=0$–5 and behaved similarly to (b) and (c) until terminated at 0.5 ms from the start of injection.

The time histories from the start of injection of these high-resolution, nonlinear simulations are compared in Fig. 4. The instability has affected the operating discharge and plasma parameters, resulting in lower discharge current and internal plasma energy. Figure 5 compares the time histories of the magnetic and kinetic energies for the $n=0I$ and $n=1I$ cases; $n=2I$ is similar to $n=1I$.

The "bursting" behavior of the energies is reflected in the structure seen in the voltage. In addition, the spikes in internal energy align with the spikes in the flow and magnetic energies (Fig. 5). When the mode is not bursting (7.9–8.6 ms), the internal energy (Fig. 4) drops: The bursting mechanism thus heats the plasma, by up to 25% in the present simulation (c.f. Fig. 4: internal energy); in the absence of bursting ($t\approx 7.5$–8.7 ms), heating due to the mode is weak. Despite this heating, the long-term evolution of the plasma results in a lower internal energy than in the axisymmetric ($n=0I$) case; the higher temperatures seen in it are due to a higher current density in the current channel as described in Sec. II C.

The poloidal-flux contours for the $n=2I$ case are shown in Fig. 6. The bursting behavior of the instability has prevented the formation of the X-points seen in the purely axisymmetric case in Figs. 2 and 3, resulting in a flux surface similar to those seen late in time after injection ceases in the more weakly driven simulations that were previously compared to the experiment.[12–14]

C. Structure of the nonlinear, unstable mode

The structure of the (nonlinear) $n=1$ mode is shown in Fig. 7 for the $n=1I$ case. The mode velocity and magnetic

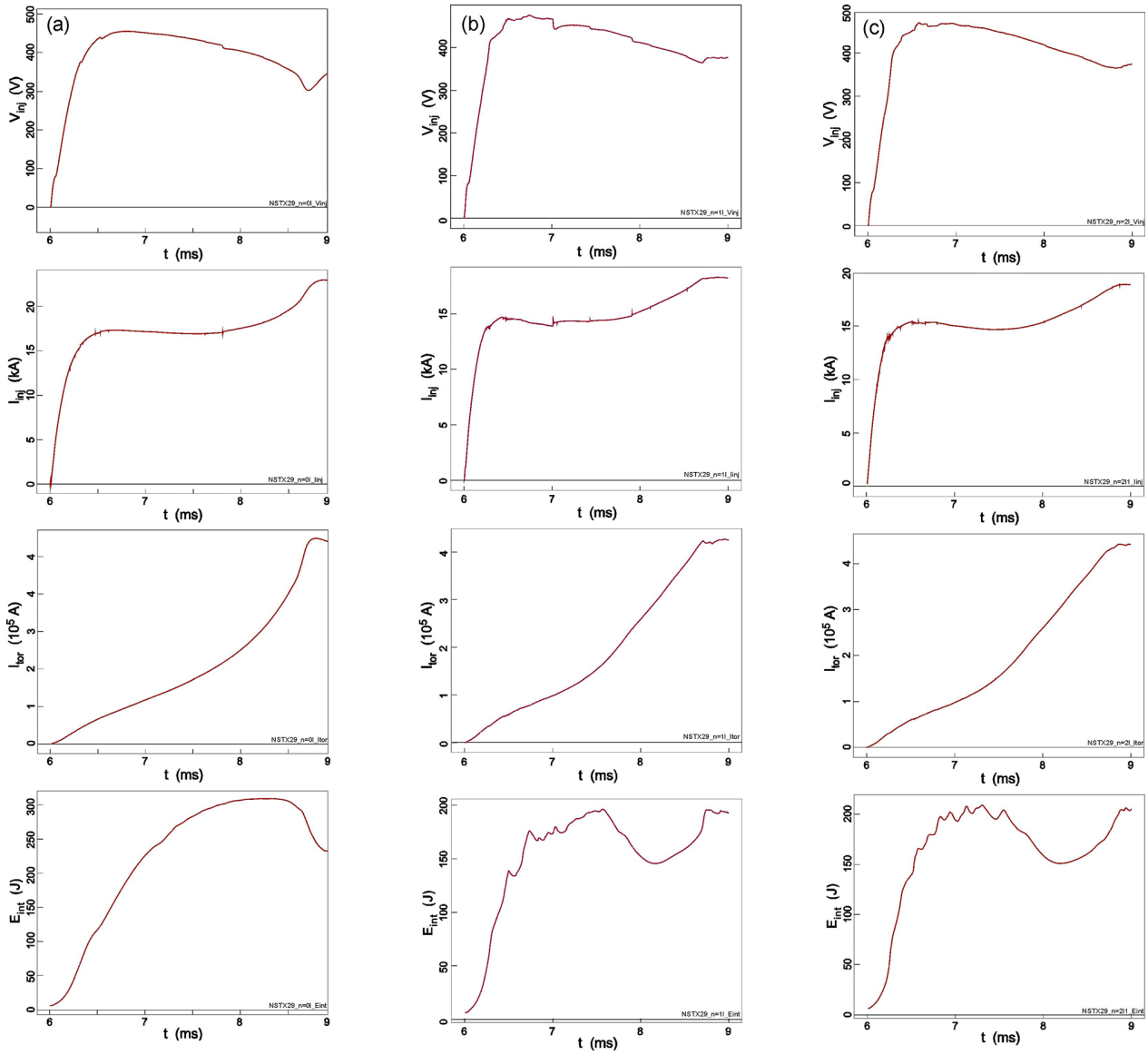

FIG. 4. Time histories of the axisymmetric and non-axisymmetric simulations. Columns, left-right: $n=0I$, $n=1I$, and $n=2I$. Rows (top-bottom: injection voltage (V), injection current (kA), toroidal current (100 kA), and internal energy (J).

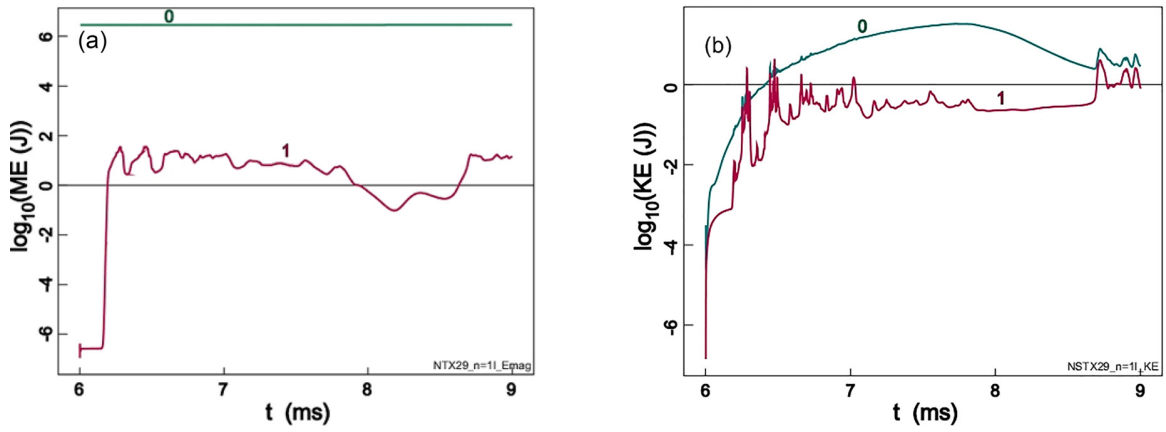

FIG. 5. (a) Magnetic and (b) kinetic energies for the $n = 1I$ case for the $n = 0$ and 1 modes.

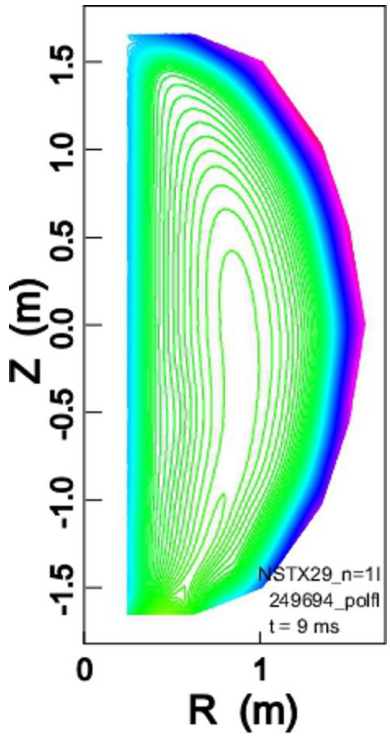

FIG. 6. Axisymmetric poloidal flux for the $n = 2I$ case, showing the lack of an X-point while helicity is injected. The injected poloidal flux is approximately the same as in the previous low-temperature simulations.[14]

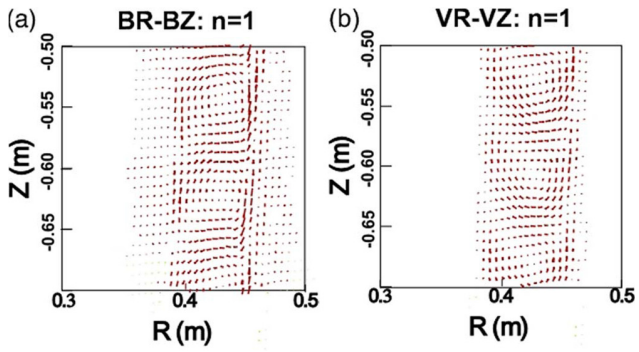

FIG. 7. Eddy structure for the $n = 1$ Fourier component of (a) the magnetic field and (b) the velocity in $n = 1I$ at 7.75 ms.

field form eddies in the poloidal plane. The eddies are oriented along the toroidal field as noted for the weakly driven simulations from Ref. 21 shown in Fig. 1. Also, the ratio of the toroidal current density (not shown) to poloidal current density in each mode is approximately the same as the ratio of the $n = 0$ magnetic fields. The perturbed current is thus flowing primarily along the total (toroidal plus poloidal) axisymmetric magnetic field. The eddies are broader in the nonlinear simulation than in the linearized calculations discussed in Section IV, although they are otherwise very similar.

One effect of the instability that is particularly noticeable is the width and structure of the axisymmetric current density, as seen in Fig. 8. The instability broadens the current channel relative to the unperturbed distribution of current density and plasma-flow. This bends the evolving poloidal magnetic field ahead of the primary current channel, contributing to the magnetic force distribution driving the flux bubble expansion.

The $n = 1$ and $n = 2$ modes in $n = 2I$ are compared in Fig. 9. The $n = 2$ wave vector along the current sheet is twice that of the $n = 1$ mode so that the relative phases of the two

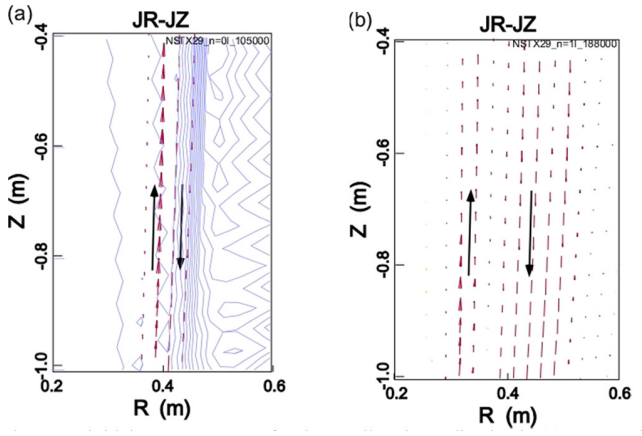

FIG. 8. Poloidal current vectors for the small major radius leg in (a) $n = 0I$. The light-blue background shows contours of the z-component of plasma flow velocity. (b) $n = 1I$ simulations. The long arrows are included to clarify the direction of current density. The net current is downward and approximately equal in the two cases. The plasma flow field (not shown in (b)) is also broadened.

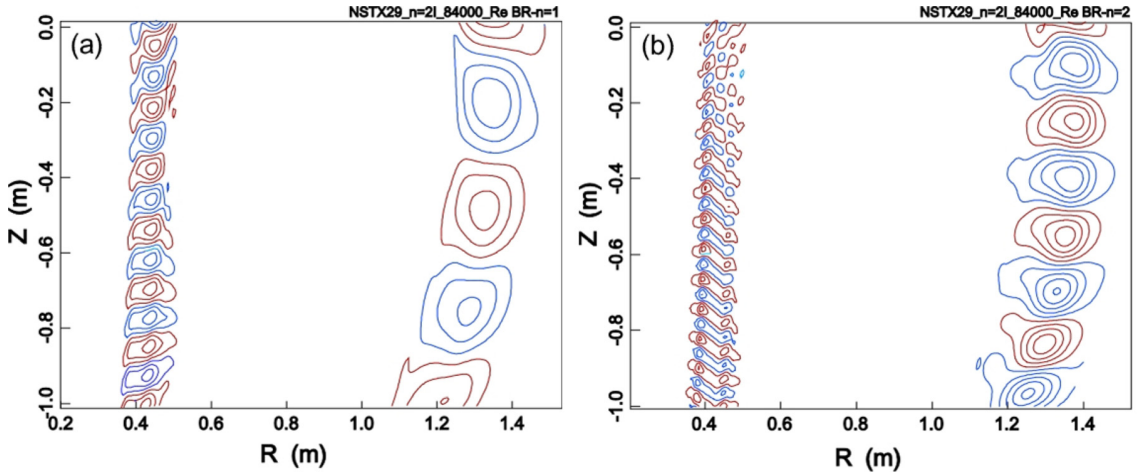

FIG. 9. Comparison of the radial magnetic field structures for (a) the $n=1$ and (b) the $n=2$ modes in $n=2I$ at 7.5 ms. Shown are the contours of B_R for the inner and outer legs of the flux bubble.

modes are the same on the inner and outer legs of the current sheet, despite significant changes in the wave vectors along the sheet, indicating that the two modes are effectively locked together.

III. LINEARIZED CALCULATIONS TO IDENTIFY THE UNSTABLE MODE

A. Linear mode growth from NIMROD studies

Linear computations of the unstable plasma-sheet mode elucidate the source of free energy and its reconnecting nature. We extract the axisymmetric part of the solution from one of the nonlinear simulations at times of interest and use those fields as the equilibrium for time-dependent linear computations, which are also run with NIMROD. This approach allows us to investigate the influence of physical parameters such as the resistivity, viscosity, and diffusivity; in addition, the $n=0$ flow can be turned off to assess its contribution to the instability.

The equilibrium in the calculations discussed below is from the axisymmetric $n=0I$, nonlinear simulation at 7.5 ms unless otherwise noted. The linear calculations used the eighth order polynomial basis functions to ensure the spatial resolution of the perturbation; convergence studies show that the growth rates are accurate to within 5%. Figure 10 shows the growth from noise of the kinetic energy (E_k) in the $n=1$ mode with a growth rate about $0.2\,\mu s^{-1}$, twice that of the mode amplitude. The linear $n=2$ kinetic-energy growth rate (not shown) approximately equals that of the $n=1$ mode. Note that Fig. 9 shows that the two modes are locked together in the nonlinear simulation.

To test the contribution of the velocity (and velocity shear) to the mode, the same calculation was run with the $n=0$ equilibrium flow field set to zero. As summarized in Table I, the growth rate for the $n=1$ mode decreased from $1.08\times10^5\ s^{-1}$ to $0.79\times10^5\ s^{-1}$ whereas the growth rate of the $n=2$ mode was unchanged. Thus, although the plasma flow contributes to the growth of the $n=1$ mode, the instability persists without the $n=0$ flow.

We separately tested the sensitivity of the mode to plasma resistivity and viscosity. The conclusion is that the values of these parameters used in the simulation have a quantitative effect on the instability; examination of the mode structure, however, showed no qualitative effects. The particle diffusion had almost no effect, indicating that the interchange instability is not playing a significant role in the present observations.[24]

The linear, $n=1$ mode structure shown in Fig. 11 is very similar to the asymmetric perturbations in the nonlinear simulation, shown in Fig. 7, with velocity vortices accompanied by magnetic field "vortices" generated by current along the magnetic field. The structures are similar, although the linear mode is narrower in poloidal width than the nonlinear behavior, where there is a significant broadening of the current channel relative to the axisymmetric nonlinear result. A comparison with the poloidal-flux structure at 7.0 ms shows that the mode is not generated in the sheet carrying the primary particle flow along the inner surface of the expanding flux bubble; instead, as observed in the nonlinear 3D evolution, the drive is along the surface of the bubble where the current is concentrated.

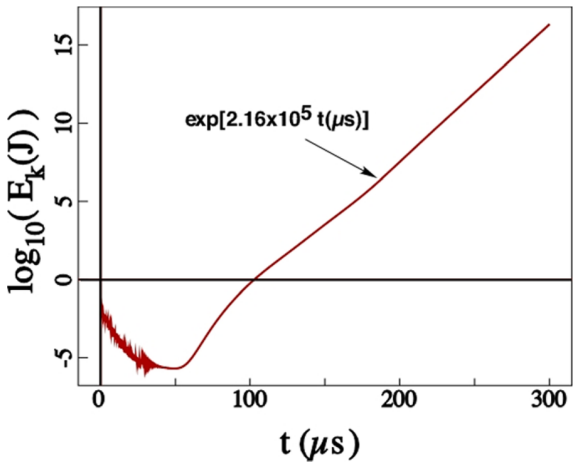

FIG. 10. Linear growth of the $n=1$ mode from noise, starting from the $n=0$ equilibrium ($n=0I$) at 7.5 ms.

TABLE I. Sensitivity of instability amplitude growth rate to numerical dissipation values.

Parameter	Base value	Test value	n = 1 growth rate (s^{-1})	n = 2 growth rate (s^{-1})
Base calculation[a]			1.08×10^5	1.16×10^5
Include equilibrium flow?	Yes	No	0.79×10^5	1.19×10^5
Kinematic viscosity	150 m^2/s	15 m^2/s	3.26×10^5	4.25×10^5
Resistivity (mag. diffusivity)	$411/T_e^{3/2}$ m^2/s	$10^4/T_e^{3/2}$ m^2/s	5.06×10^5	5.75×10^5
Particle diffusivity (holds n ≈ constant)	10^5 m^2/s	10 m^2/s	1.00×10^5	1.16×10^5

[a]All $n = 0$ quantities are kept constant except as listed.

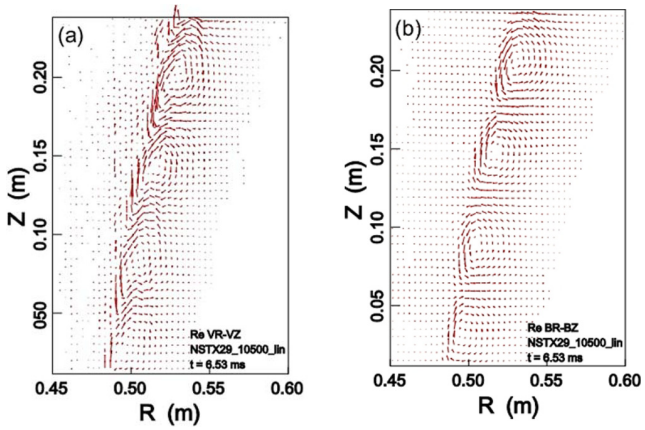

FIG. 11. Poloidal mode structure for linear, $n = 1$ calculation: (a) velocity vectors and (b) magnetic field vectors. The real parts are shown.

To elucidate this point, consider the overlay of linear eigenfunctions and equilibrium current density presented in Fig. 12. The two frames show magnetic-field vectors from linear results computed without and with the $n = 0$ flow from the nonlinear simulation. The color contours of J_ϕ/R demonstrate that the current is composed of two oppositely directed layers with the inner layer being stronger than the outer layer. The current flows primarily parallel to **B**, and the difference in the poloidal part of each layer is the net injected current as in Fig. 8. Without $n = 0$ flow (Fig. 12(a)), the perturbed magnetic field is normal to the flux-bubble surface between the two current layers. With $n = 0$ flow (Fig. 12(b)), the eigenfunction is concentrated higher in the bubble structure and is shifted onto the inner current layer. The existence of the normal-field perturbation with or without flow suggests that magnetic reconnection is a property of the linear mode, as discussed in the remainder of this section and in Sec. III B. The source of the reversed current, itself, is also of interest. Figure 1(b) shows the toroidal-flux bubble carrying poloidal flux from above the injector slot into a flux null along the inboard side of the chamber. The spatial variation of the flux function from the null region to the leading edge of the expanding bubble gives rise to the reversed-current layer in our nonlinear simulations.

To explore further the role of resistivity, a set of linearized NIMROD calculations was undertaken with the contribution of the $n = 0$ flow turned off, the resistivity uniform in space (no temperature dependence), and a low value of kinematic viscosity. The growth rate vs. resistive diffusion is shown in Fig. 13. The result is a scaling with Lundquist number to the −0.4 power, close to that expected for a resistive kink. In addition, a comparison of linear growth rates computed with and without pressure for otherwise similar equilibrium fields shows difference by no more than 10%. Considering all of the parameter dependencies presented in this section leads us to conclude that the mode is

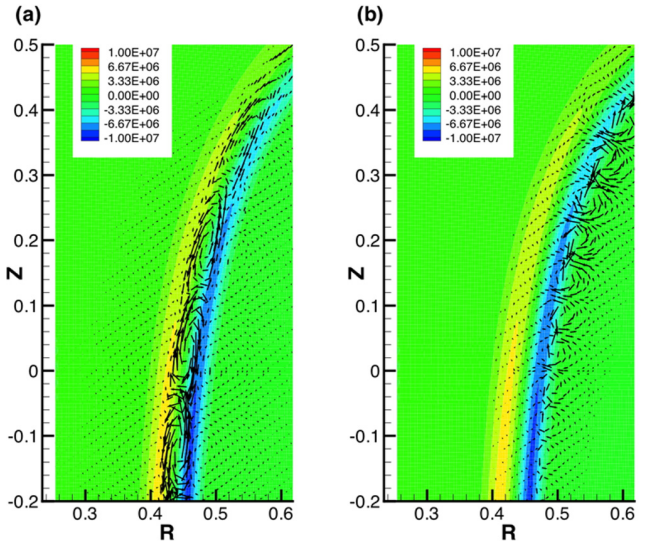

FIG. 12. Contour plots of equilibrium J_ϕ/R (A/m^3) overlaid with the vectors of the poloidal components of magnetic field from $n = 1$ linear computations computed (a) without and (b) with $n = 0$ flow.

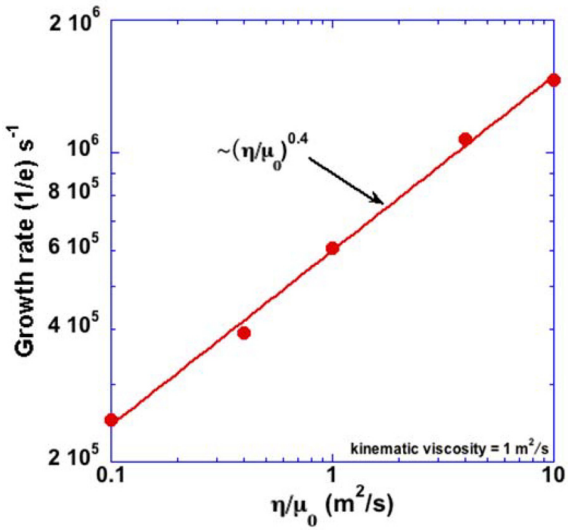

FIG. 13. Linear growth rate without the nonlinear flow contribution and with resistivity independent of temperature.

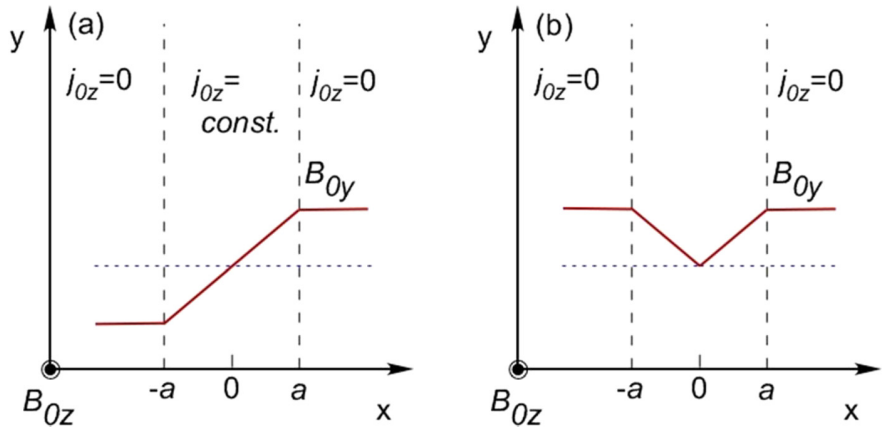

FIG. 14. (a) Slab model. The slab between $x = \pm a$ carries a constant current, j_{0z} along the z-axis, generating $B_{0y} = \mu_0 j_{0z} x$ as shown. The slab is oriented such that $B_{0y} = 0$ at $x = 0$. We neglect the small contribution to B_{0z} from the current along y. (b) Non-monotonic model. The horizontal dashed line shows $B_{0y} = 0$.

predominately a resistive kink-like, current-driven mode with contributions from the plasma flow.

There are times during the nonlinear simulations $n = 0I$ and $n = 2I$ with low $n = 1$ amplitude and no bursting (Fig. 4). Tests were made to see whether the mode is linearly stable during this time. A linear simulation starting from the $n = 0$ component of $n = 1I$ during that time interval is stable, indicating that the $n = 0$ and $n = 1$ parts of the equilibrium have evolved to a stable state including a nearly steady-state, $n = 1$ mode which does not undergo relaxation events. (Note that the nonlinear, $n = 0$ equilibrium used for this $n = 1$ simulation contains a nonlinear structure resulting from the instability.)

B. Instability drive and a slab model

To support the conclusions regarding the instability mechanism, consider the simple, static infinite-slab equilibria shown in Fig. 14. For comparison with the current sheet in toroidal computations, the z-direction of the slab configuration is aligned with $\mathbf{B}_0$ in the middle of the slab. We assume that perturbations have $\exp(iky)$ dependence over the y-z plane, i.e., no variation in z. This imposes a periodicity in y, and the perturbations are resonant at $x = 0$. The actual TCHI configuration is line-tied, but the wavelengths are much smaller than the length of field-lines within the domain, and line-tying effects diminish in the short-wavelength limit.[25] Using the energy principle, one can show that the periodic slab configuration is marginally stable to current-driven ideal MHD modes, so we focus on stability with respect to reconnecting modes. Standard Δ' analysis for resistive stability is straightforward in this basic current-sheet configuration, and the single-layer configuration (Fig. 14(a)) is considered in the seminal paper by Furth, Killeen, and Rosenbluth (FKR).[26] With an assumed large and approximately uniform z-component of $\mathbf{B}_0$, $F \equiv \mathbf{k} \cdot \mathbf{B}_0$ varies linearly in the current sheet, $-a \le x \le a$, and is uniform in each region outside the sheet. Apart from the tearing layer, the x-component of the perturbed-$\mathbf{B}$ satisfies

$$Fb_x'' - F''b_x - k^2 F b_x = 0, \tag{1}$$

where the prime indicates differentiation with respect to x. The second term vanishes within the current sheet and outside the sheets, and both b_x and $Fb_x' - F'b_x$ are continuous at $x = \pm a$.

Simplifying for distant walls, the solution over the outer ideal region in $x > 0$ is

$$b_x(x) = \begin{cases} (ka)^{-1} \sin h[k(x-a)] + \exp[-k(x-a)], & 0 < x \le a \\ \exp[-k(x-a)], & x > a, \end{cases} \tag{2}$$

and the solution is symmetric about $x = 0$. The normalized resistive-layer matching parameter is then

$$\Delta' a = \lim_{\varepsilon \to 0} a \frac{d}{dx} \ln(b_x) \Big|_{x=-\varepsilon}^{x=\varepsilon} = 2\tilde{k} \frac{\cos h(\tilde{k}) - \tilde{k} \exp(\tilde{k})}{\tilde{k} \exp(\tilde{k}) - \sin h(\tilde{k})}, \tag{3}$$

where $\tilde{k} = ka$, and the result is equivalent to Eq. (30) of FKR. Figure 15 shows this relation over $\tilde{k}$-values of interest. The solution is unstable to reconnection $(\Delta' > 0)$ for $0 \le \tilde{k} < 0.639$, and for $\tilde{k} \ll 1$, $\Delta' a \cong 2/\tilde{k}$. The piecewise linear B_{0y} profile of Fig. 14(a) is just an example, and other current-sheet distributions provide similar results. For example, with $B_{0y}(x) \sim \tan h(x/a)$, $\Delta' a = 2/\tilde{k} - 2\tilde{k}$, which is marginally stable at $\tilde{k} = 1$.[24] The unstable eigenfunction for each current-sheet profile appears similar to the plots shown in Figs. 7(b) and 11(b) from our nonlinear and linear NSTX computations.

Considering Fig. 15, the transition from small-Δ' to large-Δ' occurs within a fairly narrow range of wave numbers, which may contribute to the weak sensitivity to resistivity that is described in Section III A for the linear NSTX computations. To support this point, we have also run NIMROD computations with the monotonic linear-B_{0y} profile and find inertial-regime growth rates scaling like $S^{-0.57}$

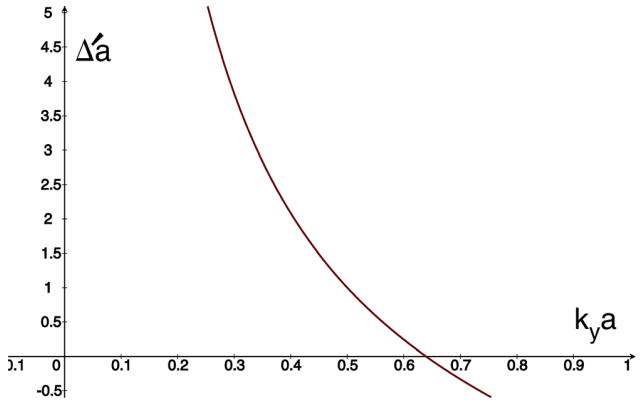

FIG. 15. Delta-prime vs. wave number from Eq. (2) for the slab model.

for $\tilde{k} = \pi/10$, i.e., nearly $S^{-3/5}$ for $\Delta' a \cong 3.5$, according to Eq. (3), and like $S^{-0.38}$ for $\tilde{k} = \pi/50$, i.e., much closer to $S^{-1/3}$ at $\Delta' a \cong 29$. Using Fig. 12, we estimate the relevant a (half-width, half-max of a single current layer) to be approximately 1 cm. The analysis using the piecewise linear B_{0y} profile predicts marginal stability for a wavelength of approximately 10 cm. With the hyperbolic-tangent B_{0y} profile, the marginal wavelength prediction is approximately 6 cm. The $n = 1$ wavelengths in Figs. 7, 11, and 12 are at least 10 cm, so there is consistency between the periodic-slab model predictions and the results of our linear and nonlinear computations. Of course, the simplified analysis does not consider effects from the flow profile in the TCHI simulations, which are found to be destabilizing, as discussed in Section III A.

For the non-monotonic B_{0y} profile (Fig. 14(b)) that is ostensibly more representative of the current profile in the nonlinear simulations, we observe that the reconnecting component of the perturbed-**B** is independent of the sign of F'. Thus, for tearing centered at the interface between the two idealized current layers, we may construct the same symmetric outer-region solution, leading to the same value of $\Delta' a$ for a given $\tilde{k}$. Current density varying within the reconnection layer would affect the inner resistive-MHD solution, but we infer that the threshold for resistive instability and the transition to large-Δ' behavior occur as they do with a single current layer. From Fig. 12(a), the eigenmode of the linear computation without $n = 0$ flow is centered between the two current layers, so the non-monotonic B_{0y} profile is more representative. Interestingly, the eigenmode with flow (Fig. 12(b)) is largely centered on the stronger upstream current layer, so the monotonic B_{0y} profile is more relevant. Of course, both piecewise linear B_{0y} profiles are idealizations.

IV. CONCLUSIONS

A high poloidal mode number, $n = 1$ instability has been observed and analyzed in resistive MHD simulations of helicity injection into the NSTX tokamak. The mode forms a narrow tube of velocity and magnetic-field vortices whose axes are aligned with the magnetic field. In simulations for which the plasma temperature is low (due to impurity radiation in the simulation model), the mode is coherent and has little effect on the injection. However, when the impurity level is reduced to a low level, the temperature in the surface layer of the injected flux bubble rises to ~100 eV or higher, and the mode amplitude undergoes relaxation oscillations. Under these conditions, the injected plasma is significantly affected, including a broadening of the current layer associated with the injected toroidal flux, generating an increase in current ahead of the bubble and heating the plasma, although the long-term evolution of the equilibrium includes injected power and results in a reduction of the internal energy relative to the axisymmetric simulation. During the relaxation events, large-scale closed magnetic flux regions seen in the injection phase of purely axisymmetric simulations do not occur.

The mode physics is examined in detail using the NIMROD code. Its linearized excitation from a fixed, axisymmetric equilibrium finds a growth rate ($\sim 0.1\,\mu s^{-1}$), which is fairly insensitive to the dissipative effects in the code (magnetic diffusivity, viscosity, and particle diffusivity). As in the nonlinear simulations, the mode is centered on the current layer at the edge of the injected flux. The velocity and magnetic-field vortices in the linear calculation are similar to those in the nonlinear simulations, although narrower in poloidal extent. The mode structure includes the component of magnetic field normal to the sheet, which implies magnetic reconnection.

To aid in the identification of the mode, the flow in the axisymmetric velocity in the nonlinear equilibrium for the linear simulation is set to zero; the mode is still unstable although at a somewhat reduced growth rate. The mode is shifted relative to the $n = 0$ current density, as seen in Fig. 12. Also, the analysis of resistive instability for a slab configuration that crudely approximates the current sheet in NSTX helps identify the unstable range of poloidal wavelengths. From this and the numerical calculations, it is concluded that the mode is predominately a current-driven resistive instability whose growth rate scaling with resistivity is close to that of a resistive kink mode. Contributions from the axisymmetric, equilibrium velocity, and/or velocity shear are not required for instability. The underlying resistive instability is the same basic current-sheet instability that is receiving renewed interest in the context of magnetic reconnection.[15–19,24] That the resulting nonlinear dynamics have greater impact as the modeled impurity concentration is reduced and temperature increases likely reflects a smaller current-sheet width at lower resistivity, which has a role in plasmoid formation.[16,17] However, during the phase of modeled active injection, the footpoints of the current channel are distant, and the instability is not part of the reconnection process that forms closed flux on the global scale. Thus, the role of the asymmetric instability reported here is distinct from that of plasmoid formation as part of the global flux-surface closure after injection, which is predicted in axisymmetric simulations of NSTX.[18,19]

To our knowledge, at the present time there are no experimental studies that can be used to determine if this mode is present in laboratory, helicity-injected plasmas. To the extent that the linear mode is current-driven, it is purely growing with no real part of the frequency and thus would

not show up as a coherent oscillation, although Doppler-shift effects could generate oscillations in the laboratory. Other physics including velocity shear (Kelvin-Helmholtz physics) and non-ideal processes not included in the slab model might also yield a real part of the frequency.

As noted, nonlinear simulations with low impurity radiation find that the mode undergoes relaxation oscillations; these would contribute to low-frequency plasma noise during the injection. Separating this from other sources of noise in experiments may be difficult. Detailed measurements, e.g., of the local magnetic field in the plasma would probably be needed to demonstrate the presence of the mode.

Consequences, if any, of the strongly driven mode for flux surface closure following helicity injection remain to be assessed in future research.

ACKNOWLEDGMENTS

This work was performed under the auspices of the U.S. Department of Energy by a subcontract to Woodruff Scientific from Lawrence Livermore National Laboratory under Contract No. DE-AC52-07NA27344 and by the PSI Center (University of Wisconsin) under Grant No. DE-FC02-05ER54813. This material is based upon the work supported by the U.S. Department of Energy, Office of Science, Office of Fusion Energy Sciences. Some of the simulations used resources of the National Energy Research Scientific Computing Center, a DOE Office of Science User Facility supported by the Office of Science of the U.S. Department of Energy under Contract No. DE-AC02-05CH11231.

[1]J. B. Taylor, Phys. Rev. Lett. **33**, 1139 (1974).
[2]J. B. Taylor, Rev. Mod. Phys. **58**, 741 (1986).
[3]M. Nagata, T. Kanki, N. Fukumoto, and T. Uyama, Phys. Plasmas **10**, 2932 (2003).
[4]T. R. Jarboe, Plasma Phys. Controlled Fusion **36**, 945 (1994).
[5]C. R. Sovinec, J. M. Finn, and D. del-Castillo-Negrete, Phys. Plasmas **8**, 475 (2001).
[6]E. B. Hooper, R. H. Bulmer, B. I. Cohen, D. N. Hill, C. T. Holcomb, B. Hudson, H. S. McLean, L. D. Pearlstein, C. A. Romero-Talamás, C. R. Sovinec, B. W. Stallard, R. D. Wood, and S. Woodruff, Plasma Phys. Controlled Fusion **54**, 113001 (2012).
[7]A. J. Redd, B. A. Nelson, T. R. Jarboe, P. Gu, R. Raman, and R. J. Smith, Phys. Plasmas **9**, 2006 (2002).
[8]A. J. Redd, T. R. Jarboe, B. A. Nelson, R. G. O'Neill, and R. J. Smith, Phys. Plasmas **14**, 112511 (2007).
[9]R. Raman, B. A. Nelson, M. G. Bell, S. Gerhardt, H. W. Kugel, B. LeBlanc, R. Maingi, and J. Menard, Phys. Rev. Lett. **97**, 175002 (2006).
[10]R. Raman, D. Mueller, S. C. Jardin, T. R. Jarboe, B. A. Nelson, M. G. Bell, S. P. Gerhardt, E. B. Hooper, S. M. Kaye, C. E. Kessel, J. E. Menard, M. Ono, V. Soukhanovskii, and NSTX Research Team, Nucl. Fusion **53**, 073017 (2013).
[11]C. R. Sovinec, A. H. Glasser, T. A. Gianakon, D. C. Barnes, R. A. Nebel, S. E. Kruger, D. D. Schnack, S. J. Plimpton, A. Tarditi, and M. S. Chu, J. Comput. Phys. **195**, 355–386 (2004).
[12]F. Ebrahimi, E. B. Hooper, C. R. Sovinec, and R. Raman, Phys. Plasmas **20**, 090702 (2013).
[13]F. Ebrahimi, R. Raman, E. B. Hooper, C. R. Sovinec, and A. Bhattacharjee, Phys. Plasmas **21**, 056109 (2014).
[14]E. B. Hooper, C. R. Sovinec, R. Raman, F. Ebrahimi, and J. E. Menard, Phys. Plasmas **20**, 092510 (2013).
[15]D. Biskamp, Phys. Fluids **29**, 1520 (1986).
[16]N. F. Loureiro, A. A. Schekochihin, and S. C. Cowley, Phys. Plasmas **14**, 100703 (2007).
[17]Y.-M. Huang and A. Bhattacharjee, Phys. Plasmas **20**, 055702 (2013).
[18]F. Ebrahimi and R. Raman, Phys. Rev. Lett. **114**, 205003 (2015).
[19]F. Ebrahimi and R. Raman, Nucl. Fusion **56**, 044002 (2016).
[20]E. B. Hooper, B. I. Cohen, H. S. McLean, R. D. Wood, C. A. Romero-Talamás, and C. R. Sovinec, Phys. Plasmas **15**, 032502 (2008).
[21]E. B. Hooper, C. R. Sovinec, R. Raman, and J. E. Menard, Bull. Am. Phys. Soc. **56**(12), 255 (2011); LLNL Report No. LLNL-POST-510511, 2011.
[22]D. E. Post, R. V. Jensen, C. B. Tarter, W. H. Grasberger, and W. A. Lokke, At. Data Nucl. Data Tables **20**, 397 (1977).
[23]R. Raman, private communication (November 2015).
[24]D. D. Ryutov, B. I. Cohen, R. H. Cohen, E. B. Hooper, and C. R. Sovinec, Phys. Plasmas **12**, 084504 (2005).
[25]Y.-M. Huang and E. G. Zweibel, Phys. Plasmas **16**, 042102 (2009).
[26]H. P. Furth, J. Killeen, and M. N. Rosenbluth, Phys. Fluids **6**, 459 (1963).